


Size-Dependent Crystalline and Magnetic Properties of 5–100 nm Fe_3O_4 Nanoparticles: Superparamagnetism, Verwey Transition, and $\text{FeO-Fe}_3\text{O}_4$ Core–Shell Formation

Shelby Klomp¹, Colby Walker¹, Mason Christiansen¹, Brittini Newbold¹, Dalton Griner¹, Yanping Cai¹, Paul Minson¹, Jeffrey Farrer¹, Stacey Smith², Branton J. Campbell¹, Roger G. Harrison², and Karine Chesnel¹ 

¹Department of Physics and Astronomy, Brigham Young University, Provo, UT 84058 USA

²Department of Chemistry and Biochemistry, Brigham Young University, Provo, UT 84058 USA

Due to their non-toxicity and their ability to be functionalized, magnetite (Fe_3O_4) nanoparticles (NPs) are good candidates for a variety of biomedical applications. To better implement their applications, it is crucial to well understand the basic structural and magnetic properties of the NPs in correlation with their synthesis method. Here, we show interesting properties of Fe_3O_4 NPs of various sizes ranging from 5 to 100 nm and the dependence of these properties on particle size and preparation method. One synthetic method based on heating $\text{Fe}(\text{acac})_3$ with oleic acid consistently gives 5 ± 1 nm NPs. A second method using the thermal decomposition of $\text{Fe}(\text{oleate})_3$ in oleic acid led to larger NPs, greater than 8 nm in size. Increasing the amount of oleic acid caused the average NP size to slightly increase from 8 to 10 nm. Increasing both the reaction temperature and the reaction time caused the NP size to drastically increase from 10 to 100 nm. Powder X-ray diffraction and electron-microscopy imaging show a pure single crystalline Fe_3O_4 phase for all NPs smaller than 50 nm and spherical in shape. When the NPs get larger than 50 nm, they notably tend to form faceted, FeO core– Fe_3O_4 shell structures. Magnetometry data collected in various field-cooling conditions show a pure superparamagnetic (SPM) behavior for all NPs smaller than 20 nm. The observed blocking temperature, T_B , gradually increases with NP size from about 25–150 K. In addition, the Verwey transition is observed with the emergence of a strong narrow peak at 125 K in the magnetization curves when larger NPs are present. Our data confirm the vanishing of the Verwey transition in smaller NPs. Magnetization loops indicate that the saturating field drastically decreases with NP size. While larger NPs show some coercivity (H_c) up to 30 mT at 400 K, NPs smaller than 20 nm show no coercivity ($H_c = 0$), confirming their pure SPM behavior at high temperature. Upon cooling below T_B , some of the SPM NPs gradually show some coercivity, with H_c reaching 45 mT at 5 K for the 10 nm NPs, indicating emergent interparticle couplings in the blocked state.

Index Terms—Magnetite nanoparticles (NPs), organic synthesis, structural properties, superparamagnetic (SPM) blocking transition.

I. INTRODUCTION

MAGNETIC nanoparticles (NPs), with typical sizes below 100 nm, are increasingly used in nanotechnologies such as magnetic recording, magneto-transport, magneto-plasmonic, and magneto-caloric effects, as well as in medical applications, such as contrast agents for MRI, hyperthermia treatment, magnetic separation, drug, and gene delivery [3], [10], [12], [15], [17], [28]. Due to its non-toxicity, strong magnetization, and high chemical reactivity, magnetite (Fe_3O_4) is well suited for these applications. In order to optimize the functionalities of magnetite NPs in the specific applications, it is important to understand and control the structural and magnetic behavior of a collection of such NPs in various temperature and magnetic environments.

Given its crystallographic structure, where Fe^{2+} and Fe^{3+} ions are distributed in an inverse spinel lattice, bulk magnetite orders ferrimagnetically below $T_c \sim 850$ K [11]. When in NP form, the internal ferrimagnetic ordering causes each particle to carry a net magnetization. Since the size of the magnetic

unit is here a few nanometers, we will refer to it as a nanospin. If the particle size is below about 125 nm [21], the particle is assumed to be magnetically monodomain, thus optimizing the magnitude of its nanospin. In addition, when the particle size is below 20 nm [22], a collection of such Fe_3O_4 NPs exhibits superparamagnetic (SPM) behavior. Upon cooling, the NPs undergo a blocking transition, typically below room temperature, where the NPs transition from a freely fluctuating SPM state to a magnetically frozen state. In addition, the magneto-crystalline structure of Fe_3O_4 may undergo a transition caused by charge ordering upon cooling, known as the Verwey transition [36]. Observed in bulk Fe_3O_4 at 125 K, this transition appears to vanish in small Fe_3O_4 NPs, depending on their size, shape, and magnetic environment [24], [26], [38]. These findings show that due to their nanostructuring, SPM Fe_3O_4 NP systems exhibit complex physical properties that strongly depend on particle size, shape, and environment. These complex properties still need to be explored at various scales, from the atomic to the nanometric and macroscopic scales.

To investigate the complex structural and magnetic properties of Fe_3O_4 NPs, a wide variety of techniques are now available and have been used, including electron microscopy [24], [40] and holography [39], magnetic force microscopy [29], Mössbauer spectrometry [14], electron paramagnetic

Manuscript received June 19, 2020; revised July 24, 2020 and August 14, 2020; accepted August 15, 2020. Date of publication August 20, 2020; date of current version October 19, 2020. Corresponding author: K. Chesnel (e-mail: kchesnel@byu.edu).

Color versions of one or more of the figures in this article are available online at <http://ieeexplore.ieee.org>.

Digital Object Identifier 10.1109/TMAG.2020.3018154

TABLE I

SUMMARY OF OUR SYNTHESIZED Fe_3O_4 NP BATCHES, LISTING THE PREPARATION METHOD, REACTION TEMPERATURE, REACTION TIME, AVERAGE PARTICLE DIAMETER ESTIMATED VIA TEM AND BLOCKING TEMPERATURE ESTIMATED VIA FC/ZFC CURVES

Batch	Method	Chemical process	Reaction T_{max}	Reaction time	Diameter (TEM)	Blocking temperature (FC/ZFC)
NP31	Fe-acac	$\text{Fe}(\text{acac})_3$ + phenyl ether + hexadecane + oleic acid + oleylamine	275 °C	30 min	5.2 ± 1.0 nm	28 K
NP20	Fe-oleate	$\text{Fe}(\text{oleate})_3$ + octadecene + 0.5 equiv. excess oleic acid	300 °C	30 min	8.6 ± 2.8 nm	50 K
NP21	Fe-oleate	$\text{Fe}(\text{oleate})_3$ + octadecene + 3 equiv. excess oleic acid	300 °C	30 min	10.1 ± 2.8 nm	110 K
NP28	Fe-oleate	$\text{Fe}(\text{oleate})_3$ + octadecene + oleic acid	295 °C	45 min	11.4 ± 2.4 nm	
NP29	Fe-oleate	$\text{Fe}(\text{oleate})_3$ + octadecene + oleic acid	310 °C	20 min	11.8 ± 1.1 nm	120 K
NP30	Fe-oleate	$\text{Fe}(\text{oleate})_3$ + octadecene + oleic acid	305 °C	60 min	14.3 ± 2.9 nm	150 K
NP32	Fe-oleate	$\text{Fe}(\text{oleate})_3$ + octadecene + oleic acid	320 °C	120 min	(Single Fe_3O_4) 13 nm (Core/shell $\text{FeO}/\text{Fe}_3\text{O}_4$): 70 nm, 85 nm	125 K (Verwey) 300 K, 320 K bumps

resonance [26], [38], muon spin resonance, magnetometry [5], [6], [31], X-ray magnetic spectroscopy [14], X-ray magnetic scattering [8], [19], [30], and neutron scattering [25]. However, given the diversity of preparation methods, and the strong dependence of particle size, shape, and properties on the synthetic method, there is still a lot to explore. Here, we present a study on a wide range of particle sizes, ranging from 5 to 100 nm, prepared by organic chemical synthesis based on the decomposition of iron oleate or iron acac in the presence of oleic acid. We explored the effect on the size and shape by varying parameters in the synthesis method, such as oleic acid amount, reaction temperature, and reaction time. We then investigated their structure, crystallinity, and their SPM behavior via magnetometry and show a consistent but drastic dependence of the magnetic characteristics on particle size.

II. CHEMICAL SYNTHESIS

The Fe_3O_4 NPs were synthesized following various organic solution methods, which are summarized in Table I. For clarity, we only present a selection of representative batches in Table I, though we emphasize that multiple repetitions of each method demonstrated reproducibility in the observed results and trends. The first method, described by Altavilla *et al.* [1], is based on the thermal decomposition of $\text{Fe}(\text{acac})_3$ in the presence of phenyl ether, hexadecane, oleylamine, and oleic acid at 275 °C for 30 min. This method consistently gave a well-controlled particle size of 5 ± 1 nm. With the solution refluxing at around 275 °C, we found that varying the reaction

temperature was challenging and did not cause a significant change in particle size. For that reason, Table I includes only one preparation batch (batch NP31) using the Fe-acac method. In order to obtain larger particle sizes, we utilized a second approach, described by Jana *et al.* [16], which is based on the thermal decomposition of iron oleate, $\text{Fe}(\text{oleate})_3$, in the presence of octadecene and oleic acid. Variations to this method were investigated by either increasing the equivalents of oleic acid, raising the reaction temperature, or increasing the reaction time.

In batches NP20 and NP21, we used the Fe-oleate method and increased the amount of oleic acid from 0.5 equivalents in excess (NP20) to 3 equivalents in excess (NP21). For both preparations, the reaction temperature was 300 °C and reaction time was 30 min. In batches NP28, NP29, NP30, and NP32, we again used the Fe-oleate method, but increased the reaction temperature from 295 °C to 320 °C, and also the reaction time from 20 up to 120 min. For all batches, once the reaction was completed, the solution was slowly cooled to room temperature, and particles were dissolved in chloroform, precipitated in ethanol, and separated by centrifugation at a speed of 5000 r/min for 15 min. After successive rounds of precipitation, a black solid was obtained, whose appearance was often wet until after being vacuum dried in a desiccator.

III. METHODS

Once fabricated, the Fe_3O_4 NPs were characterized using X-ray diffraction (XRD), transmission electron microscopy (TEM), energy dispersive X-ray (EDX) spectroscopy, and vibrating sample magnetometry (VSM).

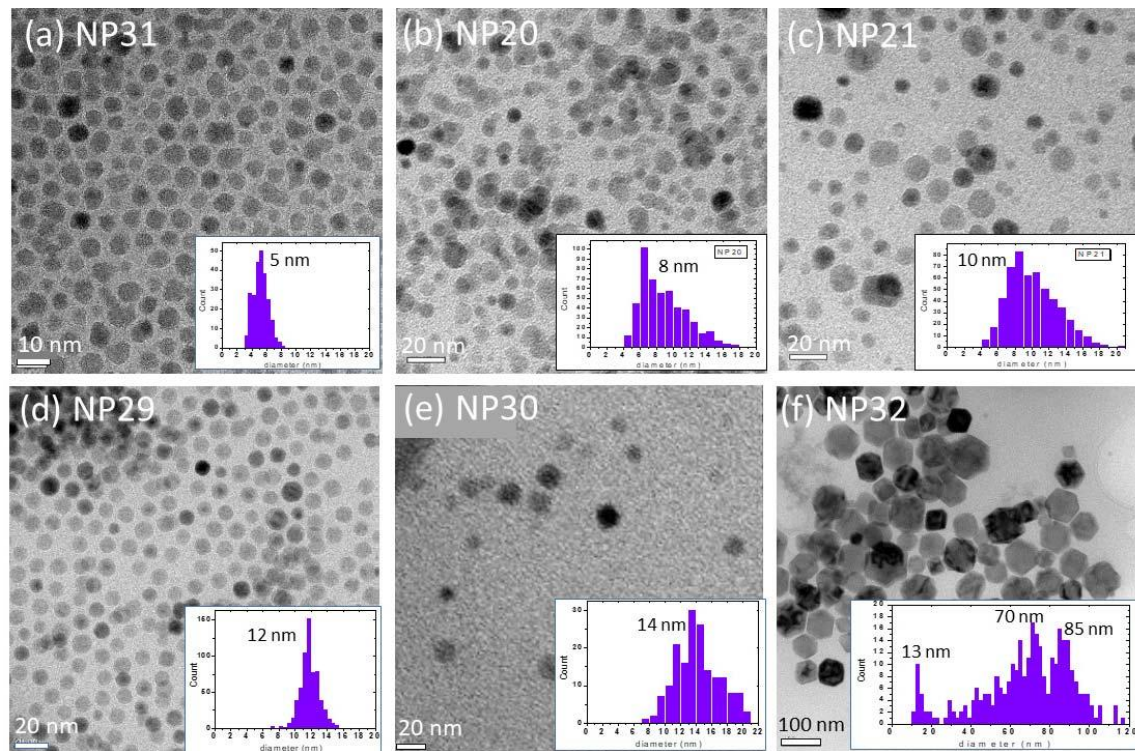


Fig. 1. Selection of bright field TEM images for the various batches of Fe₃O₄ NPs, in increasing order of size. Insets: particle size distribution calculated on several TEM images (including the showed one and other images not shown) for each batch. (a) NP31, average size 5.2 ± 1.0 nm. (b) NP20, average size 8.6 ± 2.8 nm. (c) NP21, average size 10.1 ± 2.8 nm. (d) NP29, average size 11.8 ± 1.1 nm. (e) NP30, average size 14.3 ± 2.9 nm. (f) NP32, average sizes 13 nm, 70 nm and 85 nm.

The XRD data were collected on a PANalytical X'Pert Pro MPD diffractometer with sealed tube Cu X-ray source, X'Celerator detector, and Ge monochromator. Rietveld refinements were performed using the TOPAS Academic software [9], using the line shape approach of Balzar [2] for the smaller NP31 particles and a Thompson, Cox, Hastings [35] pseudo-Voigt profile function for the larger NP32 particles.

TEM Images were acquired using a ThermoFisher Scientific Tecnai F20 UT operating at 200 kV. For the TEM measurements, the NPs were deposited on very thin carbon membrane grids by dissolving a measured amount of the NPs in powder or paste form in either chloroform or toluene and placing a drop of the solution on the membrane. The concentration of the solution was finely adjusted in order to deposit as close as possible a monolayer of NPs (too concentrated solutions lead to multilayered deposits and too diluted solutions lead to sparse NP sets). A series of TEM images were collected on each batch of NPs at various concentrations. To estimate the average NP size, hundreds of individual NPs were manually analyzed using the ImageJ software. The average particle size and size distribution were estimated using between 300 and 600 NPs for each batch. The EDX data were collected on the TEM instrument using a focused beam mode (STEM) with nominal beam diameter <1 nm. This allowed the collection of EDX spectra at different locations of the NP assemblies with a nanometric spatial resolution.

The VSM data were collected on a Quantum design physical properties measurement system (PPMS) that includes a

superconducting magnet able to produce up to 9 T and a cryogenic sample holder using liquid helium. For the VSM measurements, a small amount of the fabricated dried powder/paste was inserted into a capsule of about 1 mm³ and placed in the VSM instrument. The material was tightly compacted inside the capsule, which was itself tightly secured in place using pieces of quartz, so to prevent any motion in the VSM instrument when under vibration during the measurement. Magnetization loops were typically collected over a field range of ± 5 T. Field cooling (FC) and zero-field cooling (ZFC) measurements were typically carried out in a field of 10 mT at a warming speed of 1 K/min over the 5–400 K range. Data points were typically collected at 20 s intervals. SPM blocking transitions were identified by comparing FC and ZFC curves.

IV. STRUCTURAL AND MAGNETIC PROPERTIES

Below, the structural and magnetic properties of the Fe₃O₄ NPs measured by TEM and characterized XRD and VSM are discussed, including: the particle size and shape, the crystalline structure, the Verwey transition, the SPM blocking temperature, and the magnetization characteristics such as saturation and coercive field.

A. Particle Size and Shape

A selection of TEM images for each NP batch is shown in Fig. 1. Batch NP31 synthesized via the Fe-acac method

shows spherical particles with an average size of 5.2 ± 1.0 nm. The excellent size homogeneity causes the NPs to self-assemble in a hexagonal lattice when deposited. Batches NP20 and NP21 synthesized via the Fe-oleate method at higher temperature (300 °C) compared with the Fe-acac method (275 °C), but for the same reaction time (30 min), led to larger but more disperse particle sizes. NP20 shows an average size of 8.6 ± 2.8 nm, while NP21 (6 × oleic acid) shows an average size of 10.1 ± 2.8 nm, indicating that increasing the amount of oleic acid tends to produce larger particles, as also observed by Jana *et al.* [16]. In their report, Jana *et al.* [16] interpret this result as following: “When the fatty acid with a relatively long chain is used, such as oleic acid, the size of the monodisperse nanocrystals achieved before the Ostwald ripening stage is fixed at a certain value that is dependent on the ligand concentration” and “...the higher the ligand concentration, the larger the size of the nearly monodisperse nanocrystals.”

Batches NP28, NP29, NP30, and NP32, synthesized via the Fe-oleate method, where reaction temperature or time was further increased, all show larger particle sizes. Interestingly, batches NP28 (295 °C, 45 min) and NP29 (310 °C, 20 min) show similar average particle sizes. However, comparing the size distribution for NP28 (11.4 ± 2.4 nm) and NP29 (11.8 ± 1.1 nm) indicates that while increasing temperature and reaction time both lead to larger particles, increasing the reaction temperature provides a better control of particle size. This is confirmed with NP30 (305 °C, 60 min), where the reaction time was increased to 60 min and the particle average size increased to 14.3 ± 2.9 nm. When the reaction time is further increased to 120 min, with NP32 (320 °C, 120 min), a very wide range of particle sizes is produced, from as small as 10 nm to as big as 200 nm. In this case, it appears that the increase in temperature from 305 °C to 320 °C led to larger particles and the significantly longer reaction time led to a much wider size distribution. The overall size distribution for NP32 (calculated using over 300 particles) shows three main average sizes: 13, 70, and 85 nm. Also, while the shape of particles smaller than about 50 nm is approximately spherical, larger particles exhibit more angular shapes, such as cubic, hexagonal-parallelepipedic, or rhombohedric, with the formation of clear facets.

B. Crystalline Structure and Core–Shell Formation

The crystallinity of the NPs was probed using powder XRD as well as high-resolution transmission electron microscopy (HRTEM). XRD data collected from each of the samples were analyzed via Rietveld refinement. The results are illustrated in Fig. 2, which shows XRD patterns for the smallest particles NP31 (5 nm) and for the largest particles NP32 (up to about 100 nm). For the Fe_3O_4 phase ($Fd\bar{3}m$), the cubic cell parameter is $8.3575(15)$ Å for NP31 and $8.3973(7)$ Å for NP32, with all atoms on (x, x, x) Wyckoff sites, where x is $1/8$ for Fe(tet), $1/2$ for Fe(oct), $0.3687(4)$ for O in NP31, and $0.3630(12)$ for O in NP32. In this notation, “tet” refers to the tetrahedral sites and “oct” refers to the octahedral sites. The slight change in cell parameter for the Fe_3O_4 phase, from 8.3575 Å in NP31 to 8.3973 Å in NP32, suggests a topotactic transition,

reflecting that NP31 is overall more oxidized than NP32, and resonates with findings in [32]. For the FeO phase ($Fm\bar{3}m$), the cubic cell parameter was $4.3156(3)$ Å, with Fe at (0,0,0) and O at (1/2,0,0). Broad unidentified peaks (not from known iron-oxide phases) at $2\theta = 19.5^\circ$ and 35° were included in the model as independent Gaussian functions. Isotropic thermal parameters and full occupancies were employed for all atoms. Using the method described in [2], and assuming an approximately monodisperse size distribution, we obtain an average NP diameter of 5.3 ± 0.1 nm from the XRD peak shapes for NP31, which agrees very well with the estimate of 5.2 nm from TEM images. For the NP32 sample, which has a very broad NP size distribution in the range from 10 to 100 nm, as seen in Fig. 1(f), a meaningful estimate of average diameter requires some advanced knowledge of the shape of the distribution, which we do not have.

The XRD data for NP31 [Fig. 2(a)] reveal a nearly pure 100% Fe_3O_4 phase. Since the XRD data were collected between one and three years after the samples were synthesized, we were concerned about possible oxidation to Fe_2O_3 . Indeed, it has been shown that oxidation of Fe_3O_4 NPs likely impacts their crystalline and magnetic properties [33], [34]. However, in the present work, no significant trace of Fe_2O_3 , either as maghemite or hematite, was detected in the Rietveld refinements in any of the samples, including NP31 and NP32. The observed stability of our Fe_3O_4 NPs is likely due to storing them under mild vacuum in desiccators shortly after their fabrication.

The HRTEM images of NP31, illustrated in Fig. 2(b), confirm that the mostly spherical particles are monocrystalline. The same result was observed for all of the NP batches, except NP32.

Interestingly, the XRD diffractogram for NP32 [Fig. 2(d)] showed an unexpected structure, indicating up to 94% of FeO mixed with 6% of Fe_3O_4 . In addition, HRTEM images of NP32 revealed that many of the largest particles, typically larger than 50 nm, exhibit a core–shell structure. As an illustration, Fig. 2(e) shows one of these particles, with a faceted shape and a largest diameter of around 75 nm, where a shell of about 7 nm is clearly visible. To identify the crystalline phases in the core and the shell, respectively, energy dispersive X-ray (EDX) spectroscopy was carried out at different locations on the shell [Fig. 2(f)] and on the core [Fig. 2(g)]. The magnitude of the EDX peaks at the various absorption edges depends on several parameters set by the electron absorption/X-ray emission process, as well as the in-depth structure and composition of the material being probed, so comparing the absolute peak magnitude does not allow to directly determine the phase. However, a comparison of the respective peak magnitudes at the core and at the shell allows seeing which locations are richer in Fe or in O, and ultimately drawing conclusion about the location of the FeO and Fe_3O_4 phases, respectively. Averaged over several particles, the ratio of the signal at the Fe K -edge (around 7.1 keV) and the O K -edge (around 530 eV) increases significantly from about 1:1 at the shell to around 2:1 at the core location. More precisely, the core/shell ratio of these Fe/O signal ratios was measured to be around 1.8 with a standard deviation of 0.2.

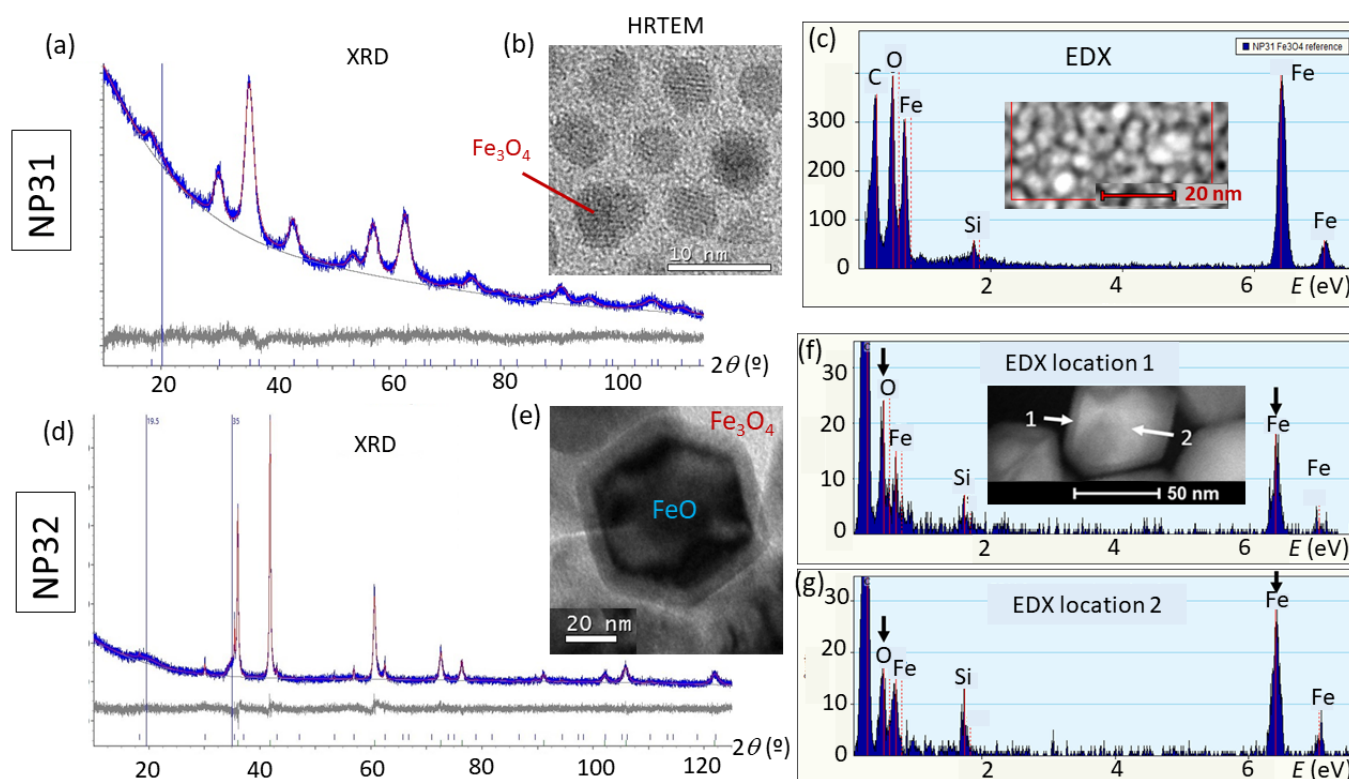


Fig. 2. (a) and (c) Structural properties of NP31 (5 nm particles). (a) XRD data with Rietveld refinement showing a pure 100% Fe₃O₄ phase. (b) HRTEM view of the particles showing single crystalline particles, assembling in a hexagonal lattice. (c) EDX spectrum collected on about a hundred of particles showing the signal at the oxygen *K*-edge and at the Fe *K,L*-edges. (d)–(g) Structural properties of NP32 (broad 10–100 nm range of particles). (d) XRD data with Rietveld refinement showing a mixture of about 94% FeO with 6% Fe₃O₄ phases. (e) HRTEM view of a ~75 nm particle showing a core-shell structure. (f) EDX spectrum collected on the shell region. (g) EDX spectrum collected on the core region. The signal ratio between the Fe and O *K*-edges suggests a core richer in iron than the shell.

This suggests that the core is richer in Fe compared with the shell, indicating the core is made of FeO and the shell of Fe₃O₄. For comparison, the EDX spectrum collected on the small NP31 particles [Fig. 2(c)] is similar to the spectrum collected on the shell of the NP32 particles. The unexpected formation of core-shell structures with our fabrication method is likely caused by lack of oxygen and reductive conditions in the core that reduce all of the Fe(III) ions to Fe(II) ions. Other fabrication methods, based on the decomposition of iron oleate via ketonic decarboxylation, have been used to produce FeO/Fe₃O₄ core-shell NPs in the range of 13–25 nm [18], [20]. The formation of FeO/Fe₃O₄ core-shell particles in the range of 50–100 nm in the present study provides complementary data and broadens the range of NP sizes for the size dependence study.

C. SPM Blocking Transition

While magnetite Fe₃O₄ orders ferrimagnetically (FIM) below its Curie temperature of $T_C \sim 850$ K, FeO is paramagnetic (PM) at room temperature and transitions into its antiferromagnetic (AFM) phase below its Néel temperature of $T_N \sim 200$ K [20]. The coexistence of these magnetic phases causes all of our Fe₃O₄ NPs and core-shell FeO/Fe₃O₄ NPs to exhibit a substantial magnetization and to collectively show an SPM-like behavior. A selection of FC/ZFC curves measured for each

NP batch is shown in Fig. 3. The FC/ZFC curves reveal an SPM blocking transition, where the NPs are in an SPM state at high temperature and enter a magnetically blocked state upon cooling below a blocking temperature T_B . Our estimate of T_B is based on the peak location in the ZFC curve—which, for most samples, approximately coincides with the merging point with the associated FC curve. While commonly adopted, this approach may yield a slight overestimate of T_B (more rigorously located somewhat below the ZFC peak) [23], but should not significantly affect the overall trend of T_B with respect to parameters such as particle size. Note that we do not use the estimates of T_B to quantify other physical properties (such as the anisotropy constant) but instead focus on the trend of T_B with particle size. Therefore, in order to be consistent with earlier experimental estimates, we choose to use the ZFC peak position to estimate T_B .

We observe that T_B consistently increases with particle size. The ZFC peak is the narrowest and its position is the lowest for the 5 nm particles, which also have the narrowest size distribution. The blocking temperature T_B , also plotted in Fig. 4(c), drastically and consistently increases from 28 K (for 5 nm particles) to 150 K (for 14 nm particles). The FC/ZFC curves for batch NP32, which exhibits a wide mix of particle sizes, show several peaks and bumps, suggesting a blocking-like behavior where the blocking temperature is still highly correlated with particle size. This suggests that even

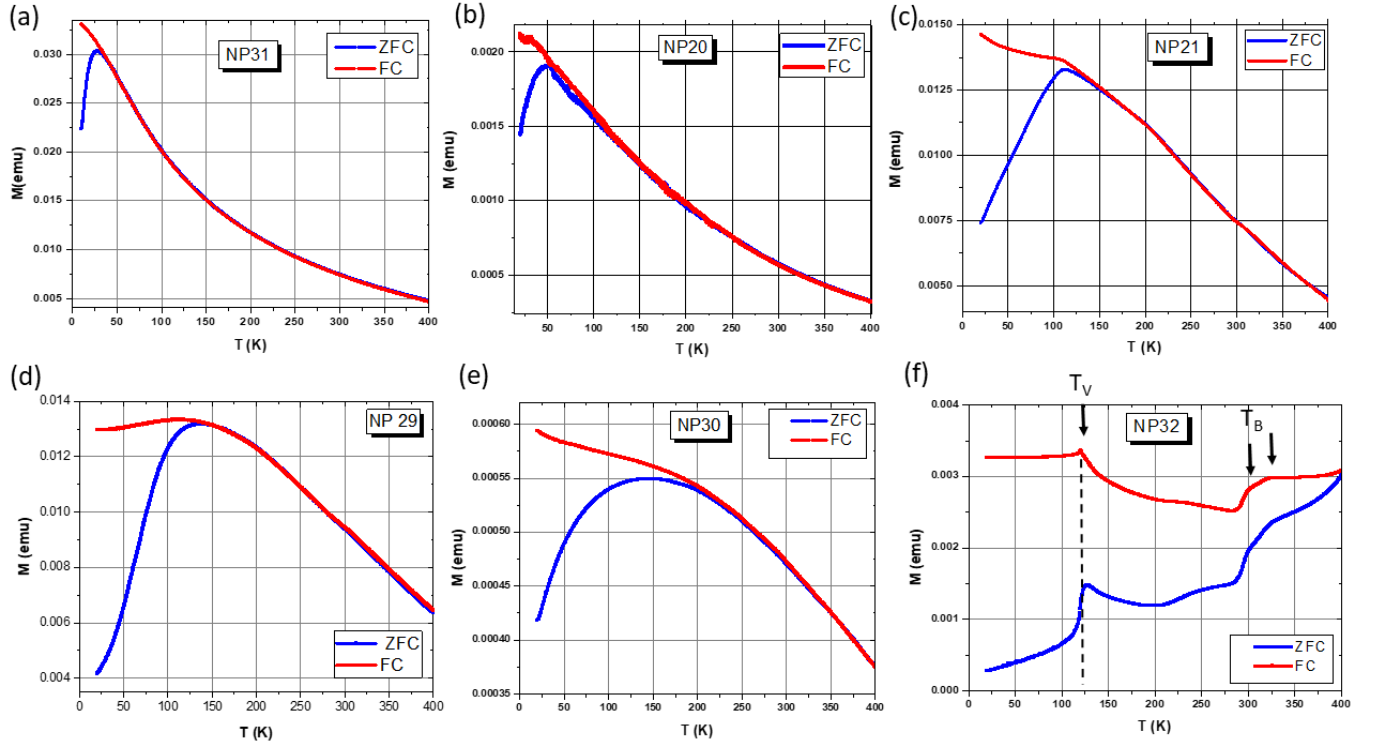


Fig. 3. Sets of FC/ZFC curves measured at 10 mT on the various batches of Fe_3O_4 NPs, in increasing order of size: (a) NP31 (5.2 nm), (b) NP20 (8.6 nm), (c) NP21 (10.1 nm), (d) NP29 (11.8 nm), (e) NP30 (14.3 nm), and (f) NP32 (10–100 nm).

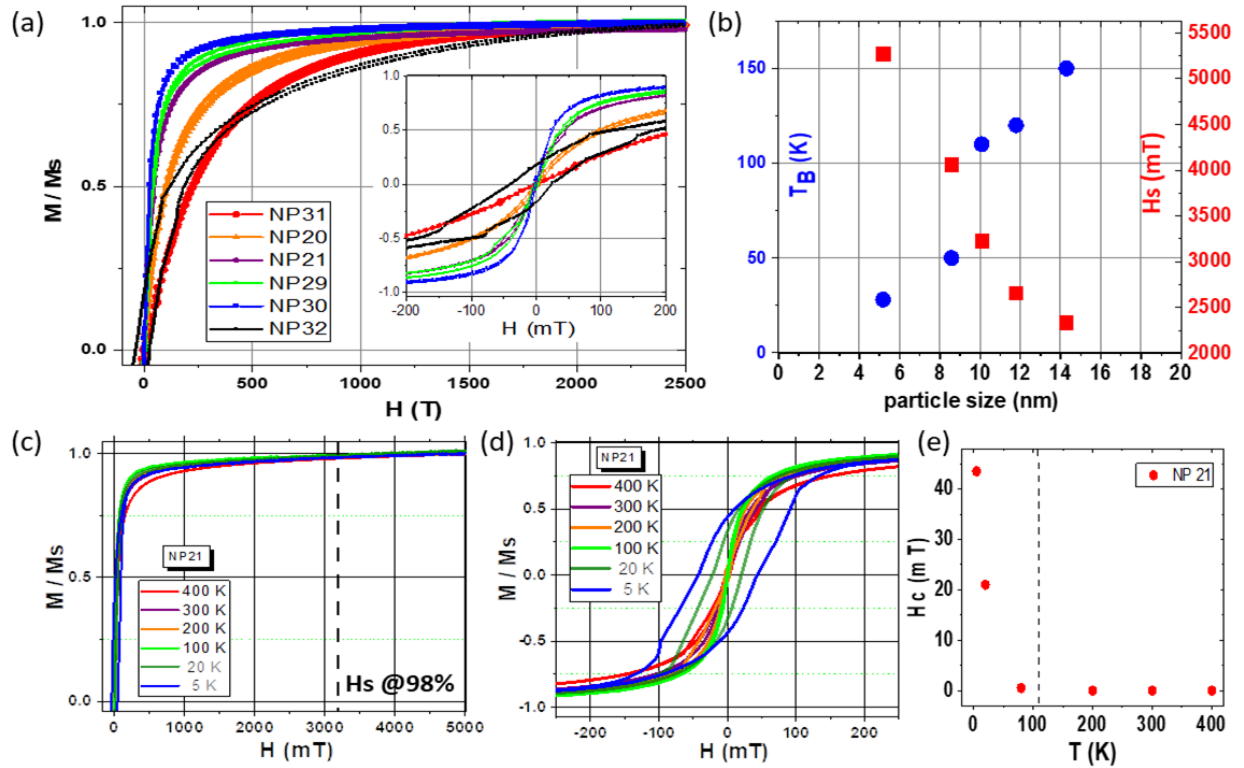


Fig. 4. (a) Normalized magnetization loops measured at 400 K for the various Fe_3O_4 NP batches (showing the positive branch only). The saturation field $H_S = H_{0.98}$ estimated when $M/M_s = 0.98$ is plotted in graph (b). Inset: zoomed-in view over a ± 200 mT range showing pure SPM behavior (no hysteresis) for all particle sizes, except NP32 which shows a coercive field $H_c \approx 30$ mT. (b) Plot of the blocking temperature T_B (in blue color) as a function of particle size in the 0–20 nm range. T_B is here estimated from the FC/ZFC curves shown in Fig. 3. (c) and (d) Selection of magnetization loops at various temperatures from 5 to 400 K for NP21 (10 nm particles). (e) Full view over the field range 0–5 T showing the asymptotic behavior toward saturation. (d) Zoomed-in view over a ± 250 mT field range. (e) Associated coercive field H_c versus temperature, confirming the SPM transition for NP21.

for the core–shell NPs, in which the PM ordered FeO core does not contribute to any spontaneous magnetization above 200 K, the FIM ordering in the Fe₃O₄ shell yields non-zero nanospins. Magnetic couplings between these nanospins lead to blocking-like behaviors, as also observed in the Lak *et al.*'s study [20].

D. Verwey Transition

The prominent narrow peak at 125 K in Fig. 3(f) is a clear sign of the Verwey transition, a magneto-crystalline transition established in bulk Fe₃O₄ [36], [37] and here observed in an NP assembly containing particles as big as 100 nm. The shape, magnitude, and sharpness of the peak at $T_v = 125$ K clearly indicate that it does not correspond to a SPM transition but is a signature of the Verwey transition. Not observed in any of the other samples, the occurrence of the strong narrow peak at 125 K in the FC/ZFC data for NP32 confirms that the Verwey transition, traditionally observed in bulk Fe₃O₄, vanishes in Fe₃O₄ NPs smaller than about 20–50 nm, depending on shape and fabrication conditions [14], [24], [38]. Due to the difficulty of observing the Verwey transition in small NPs, very few studies report it. One magnetometry study [14] reports the observation of the Verwey transition in 50 and 150 nm Fe₃O₄ particles based on a small kink in the ZFC curve, located at 16 and 98 K, respectively, temperature points well below the expected 125 K for the Verwey transition. In our study, the peak is observed at 125 K exactly both in the ZFC and the FC curves, confirming the occurrence of the Verwey transition in our batch of larger NPs (NP32).

Also, the emergence of the Verwey transition in NP32 may be associated with the formation of faceted NPs as shown in the TEM image in Figs. 1(f) and 2(e). It has been reported [24] that when comparing magnetometry data between faceted and spherical (non-faceted) Fe₃O₄ NPs of the same size (in the range of 5–15 nm), the faceted ones showed indication of the Verwey transition (kink in the ZFC curve near 120 K), whereas spherical non-faceted ones did not. The unprecedented observation of a sharp narrow peak at 125 K in our FC/ZFC data confirms existence of the Verwey transition in larger faceted Fe₃O₄ NPs. The higher temperature bumps in the FC/ZFC curve for NP32 suggest at least two additional SPM transitions, at about 300 and 320 K, corresponding to the 70 and 85 nm particle sizes, in addition to the Verwey transition peak.

Overall, the plot in Fig. 4(c) suggests that, present in all Fe₃O₄ NP assemblies, the blocking temperature T_B strongly depends on particle size. It gradually increases from 28 K for 5 nm particles to 150 K for 15 nm particle and, if extrapolated to larger particles, reaches up to 300 K for 80 nm particles.

E. Magnetic Saturation

The magnetic response of the Fe₃O₄ NPs to the application of an external magnetic field is illustrated in Fig. 4. In particular, Fig. 4(a) shows magnetization loops (showing the positive branch only for positive field $H > 0$) collected at 400 K for the different NP batches. These loops all exhibit an overall smooth s-shaped curve (which can be approximated as a Langevin

function), with little to no hysteresis, typical of SPM behavior. After normalization to magnetization at saturation M_s , they indicate that saturation depends strongly on particle size. The ‘saturating’ field $H_S = H_{0.98}$, here, estimated at 98% saturation (i.e., when normalized magnetization $M/M_s = 0.98$) at 400 K, plotted as a function of particle size in Fig. 4(c), indicates a drastic decrease from about 5200 mT for 5 nm particles down to 2250 mT for 14 nm particles. The same trend is observed at other temperatures including ambient temperature 300 K. At a fixed temperature, the nanospins carried by smaller particles require a stronger external magnetic field to be collectively aligned than do the nanospins of larger particles. This trend is mainly due to thermal effects being stronger than the external magnetic dipolar energy, easing magnetic flipping fluctuations for smaller particles (compared with larger particles) at given temperature and field. This subtle energy balance explains the lower blocking temperature for smaller particles.

F. Magnetic Coercivity

To further characterize their SPM behavior, we looked at the magnetic coercivity of our NPs. The inset in Fig. 4(a) shows a zoomed-in view of the 400 K magnetization loops around the origin (over a ± 200 mT range). No hysteresis (coercive field $H_c = 0$) is observed for any particle, except for batch NP32. The absence of hysteresis confirms a pure SPM behavior for particle sizes smaller than at least 15 nm, as also observed by Li *et al.* [22]. In their study conducted on cubic-like Fe₃O₄ NPs, Li *et al.* [22] report a particle size limit for SPM behavior to be around 20 nm using the coercivity criterion. They observed the emergence of non-zero H_c for particles larger than 20 nm, reaching up to $H_c = 20$ mT for 76 nm particles at 300 K. In the present study, we as well saw hysteresis emerge for the larger particle sizes (including up to 100 nm) with H_c reaching up to 30 mT at 400 K. While particle shape and environment are significant factors, these complimentary studies tend to indicate that the SPM behavior and the emergence of magnetic coercivity are most strongly affected by particle size.

Upon cooling below their blocking temperature, smaller NPs, which behave purely SPM at high temperature, progressively show some magnetic coercivity. A selection of magnetization loops collected at various temperatures through the blocking transition is shown for an intermediate particle size, 10 nm (NP21) in Fig. 4(c) and (d). At high temperature, above T_B , the loops are smooth without hysteresis, whereas at low temperature below T_B , hysteresis occurs. The coercive field H_c plotted as a function of temperature in Fig. 4(e) shows a drastic drop from 45 mT at 5 K down to 20 mT at 20 K, and eventually to zero above $T_B = 110$ K. The smooth shape of the loop and absence of hysteresis above T_B is characteristic of SPM behavior. The occurrence of hysteresis and a significant coercivity below T_B indicates interparticle magnetic couplings. As shown in an earlier study [6], smaller 5 nm particles do not show significant hysteresis. Hysteresis seem to occur for particles larger than 8 nm, and coercivity increases with particle size. The increased coercivity leads to

stronger remanence effects, where the magnetization M of the material does not completely return to zero when the applied magnetic field is released back to zero. Consequently, one may need to account for magnetic history when manipulating larger (10–100 nm) Fe_3O_4 NPs with an external magnetic field, in particular for applications where the net magnetization needs to be switched on and off.

V. CONCLUSION

By implementing variations of an organic solution method based on the thermal decomposition of either iron acac or iron oleate in the presence of oleic acid, we have successfully synthesized Fe_3O_4 NPs covering a wide range of sizes from 5 up to 100 nm. We found that the average particle size can be increased by increasing either the amount of oleic acid, the reaction temperature, or the reaction time. However, particle size is most sensitive to increasing temperature. The size distribution tends to be relatively wider for larger particles. Smaller particles, below 50 nm in diameter, are generally spherical. When their size exceeds 50 nm, the particles tend to form facets. In addition, the specific procedure we used to create larger particles led to the formation of core-shell structures with the core made of FeO and the shell made of Fe_3O_4 . The thickness of the shell is typically in the 5–10 nm range for core diameters in the 50–100 nm range.

We characterized the collective magnetic properties of the NPs and found that all the small particles show an SPM-like behavior at 400 K and transition into a blocked state upon cooling. The blocking temperature T_B estimated via FC measurements gradually increases from 28 K for 5 nm particles to about 150 K for 15 nm particles. A blocking-like behavior is also observed for larger particles, with T_B reaching 320 K or room temperature for particles in the 75–100 nm range. In addition, the Verwey transition at $T_v = 125$ K is clearly observed in the largest-particle batch, which contained faceted particles as big as 100 nm. Above T_B , all NPs smaller than 20 nm show a smooth magnetization curve absent of hysteresis, confirming their pure SPM behavior. Only larger particles (up to 100 nm) show significant hysteresis at high temperature up to 30 mT at 400 K. For the SPM NPs larger than about 8 nm, however, hysteresis gradually emerges upon cooling below T_B . For the 10 nm particles, the amount of coercivity reaches up to 50 mT at 5 K. At given temperature, the amount of coercivity increases with particle size.

These preliminary characterizations suggest that particle size, size distribution, temperature, and magnetic history are crucial parameters to account for when manipulating magnetite NPs under specific temperature and field environments. Improved control of the particle size in the fabrication process will allow refined studies of the blocking SPM and Verwey transitions, as well as the formation of core-shell structures, and their dependence on particle size. In addition, complementary tools such as Mossbauer and EXAFS [13], [27], will greatly increase our understanding of the local chemical and crystalline structures of Fe_3O_4 NPs versus FeO/ Fe_3O_4 core-shell particles. Such structural and magnetic information will be important for further investigations by synchrotron

X-ray, neutron, and muon-spin resonance of spatiotemporal behaviors at the atomic and nanometric scales in magnetic NPs [7], [8], [19]. The dynamics of nanoscale fluctuations in magnetic NP assemblies are particularly important aspects in nanotechnology and biomedical applications.

ACKNOWLEDGMENT

This work was supported by the Office at Creative Research and Activities and the College of Physical and Mathematical Sciences at Brigham Young University (BYU). The work of Shelby Klomp was supported by the National Science Foundation for the Research Experience for Undergraduate program under Grant #1757998 at BYU.

REFERENCES

- [1] C. Altavilla, E. Ciliberto, D. Gatteschi, and C. Sangregorio, "A new route to fabricate monolayers of magnetite nanoparticles on silicon," *Adv. Mater.*, vol. 17, no. 8, pp. 1084–1087, 2005.
- [2] D. Balzar, "Profile fitting of X-ray diffraction lines and Fourier analysis of broadening," *J. Appl. Crystallogr.*, vol. 25, no. 5, pp. 559–570, Oct. 1992.
- [3] C. C. Berry and A. S. G. Curtis, "Functionalisation of magnetic nanoparticles for applications in biomedicine," *J. Phys. D, Appl. Phys.*, vol. 36, no. 11, pp. R198–R208, 2003.
- [4] Y. Cai *et al.*, "Orbital and spin moments of 5 to 11 nm Fe_3O_4 nanoparticles measured via X-ray magnetic circular dichroism," *J. Appl. Phys.*, vol. 115, no. 17, 2014, Art. no. 17B537.
- [5] G. Cheng, C. Dennis, R. Shull, and A. R. H. Walker, "Probing the growth and aging of colloidal cobalt nanocrystals: A combined study by transmission electron microscopy and magnetic measurements," *Cryst. Growth Des.*, vol. 9, no. 8, pp. 3714–3720, 2009, doi: [10.1021/cg900426j](https://doi.org/10.1021/cg900426j).
- [6] K. Chesnel, M. Trevino, Y. Cai, J. M. Hancock, S. J. Smith, and R. G. Harrison, "Particle size effects on the magnetic behaviour of 5 to 11 nm Fe_3O_4 nanoparticles coated with oleic acid," in *Proc. J. Phys., Conf.*, vol. 521, 2014, Art. no. 012004.
- [7] K. Chesnel, A. Safsten, M. Rytting, and E. E. Fullerton, "Shaping nanoscale magnetic domain memory in exchange-coupled ferromagnets by field cooling," *Nature Commun.*, vol. 7, no. 1, p. 11648, Sep. 2016.
- [8] K. Chesnel *et al.*, "Unraveling nanoscale magnetic ordering in Fe_3O_4 nanoparticle assemblies via X-rays," *Magnetochemistry*, vol. 4, no. 4, p. 42, 2018, doi: [10.3390/magnetochemistry4040042](https://doi.org/10.3390/magnetochemistry4040042).
- [9] A. A. Coelho, J. Evans, I. Evans, A. Kern, and S. Parsons, "The TOPAS symbolic computation system," *Powder Diffraction*, vol. 26, no. S1, pp. S22–S25, Dec. 2011.
- [10] M. De and P. S. Gosh, "Application of nanoparticles in biology," *Adv. Mater.*, vol. 20, pp. 4225–4241, 2008.
- [11] M. E. Fleet, "The structure of magnetite," *Acta Cryst.*, vol. 37, no. 4, pp. 917–920, 1981.
- [12] N. A. Frey, S. Peng, K. Cheng, and S. Sun, "Magnetic nanoparticles: Synthesis, functionalization, and applications in bioimaging and magnetic energy storage," *Chem. Soc. Rev.*, vol. 38, pp. 2532–2542, Jun. 2009.
- [13] R. Gabbasov *et al.*, "Mössbauer, magnetization and X-ray diffraction characterization methods for iron oxide nanoparticles," *J. Magn. Magn. Mater.*, vol. 380, pp. 111–116, Apr. 2015.
- [14] G. F. Goya, T. S. Berquó, F. C. Fonseca, and M. P. Morales, "Static and dynamic magnetic properties of spherical magnetite nanoparticles," *J. Appl. Phys.*, vol. 94, no. 5, pp. 3520–3528, Sep. 2003.
- [15] R. Hergt, S. Dutz, R. Müller, and M. Zeisberger, "Magnetic particle hyperthermia: Nanoparticle magnetism and materials development for cancer therapy," *J. Phys., Condens. Matter*, vol. 18, no. 38, pp. S2919–S2934, Sep. 2006.
- [16] N. R. Jana, Y. Chen, and X. Peng, "Size- and shape-controlled magnetic (Cr, Mn, Fe, Co, Ni) oxide nanocrystals via a simple and general approach," *Chem. Mater.*, vol. 16, no. 20, pp. 3931–3935, 2004.
- [17] Y. Jun, J. Lee, and J. Cheon, "Chemical design of nanoparticle probes for high-performance magnetic resonance imaging," *Angew. Chem. Int. Ed.*, vol. 47, no. 28, pp. 5122–5135, Jun. 2008.

- [18] D. W. Kavich, J. H. Dickerson, S. V. Mahajan, S. A. Hasan, and J. H. Park, "Exchange bias of singly inverted FeO/Fe₃O₄ core-shell nanocrystals," *Phys. Rev. B, Condens. Matter*, vol. 78, Nov. 2008, Art. no. 174414.
- [19] J. B. Kortright, O. Hellwig, K. Chesnel, S. Sun, and E. E. Fullerton, "Interparticle magnetic correlations in dense Co nanoparticle assemblies," *Phys. Rev. B, Condens. Matter*, vol. 71, no. 1, Jan. 2005, Art. no. 012402.
- [20] A. Lak *et al.*, "Size dependent structural and magnetic properties of FeO-Fe₃O₄ nanoparticles," *Nanoscale*, vol. 5, pp. 12286–12295, Oct. 2013.
- [21] D. L. Leslie-Pelecky and R. D. Rieke, "Magnetic properties of nanostructured materials," *Chem. Mater.*, vol. 8, pp. 1770–1783, 1996.
- [22] Q. Li, C. W. Kartikowati, S. Horie, T. Ogi, T. Iwaki, and K. Okuyama, "Correlation between particle size/domain structure and magnetic properties of highly crystalline Fe₃O₄ nanoparticles," *Sci. Rep.*, vol. 7, no. 1, p. 9894, Dec. 2017.
- [23] K. L. Livesey, S. Ruta, N. R. Anderson, D. Baldomir, R. W. Chantrell, and D. Serantes, "Beyond the blocking model to fit nanoparticle ZFC/FC magnetisation curves," *Sci. Rep.*, vol. 8, no. 1, p. 11166, Dec. 2018.
- [24] A. Mitra, J. Mohapatra, S. S. Meena, C. V. Tomy, and M. Aslam, "Verwey transition in ultrasmall-sized octahedral Fe₃O₄ nanoparticles," *J. Phys. Chem. C*, vol. 118, no. 33, pp. 19356–19362, 2014.
- [25] D. Mishra, O. Petravic, A. Devishvili, K. Theis-Bröhl, B. P. Toperverg, and H. Zabel, "Polarized neutron reflectivity from monolayers of self-assembled magnetic nanoparticles," *J. Phys., Condens. Matter*, vol. 27, no. 13, Apr. 2015, Art. no. 136001.
- [26] V. N. Nikiforov *et al.*, "Magnetism and verwey transition in magnetite nanoparticles in thin polymer film," *J. Alloys Compounds*, vol. 569, pp. 58–61, Aug. 2013.
- [27] B. Pacakova *et al.*, "The internal structure of magnetic nanoparticles determines the magnetic response," *Nanoscale*, vol. 9, no. 16, pp. 5129–5140, 2017.
- [28] Q. A. Pankhurst, N. T. K. Thanh, S. K. Jones, and J. Dobson, "Progress in applications of magnetic nanoparticles in biomedicine," *J. Phys. D, Appl. Phys.*, vol. 42, no. 22, Nov. 2009, Art. no. 224001.
- [29] V. F. Puentes, P. Gorostiza, D. M. Aruguete, N. G. Bastus, and A. P. Alivisatos, "Collective behaviour in two-dimensional cobalt nanoparticle assemblies observed by magnetic force microscopy," *Nature Mater.*, vol. 3, no. 4, pp. 263–268, Apr. 2004.
- [30] J. Rackham *et al.*, "Modeling inter-particle magnetic correlations in magnetite nanoparticle assemblies using X-ray magnetic scattering data," *AIP Adv.*, vol. 9, no. 3, Mar. 2019, Art. no. 035033, doi: [10.1063/1.5080155](https://doi.org/10.1063/1.5080155).
- [31] A. G. Roca, M. P. Morales, K. O'Grady, and C. J. Serna, "Structural and magnetic properties of uniform magnetite nanoparticles prepared by high temperature decomposition of organic precursors," *Nanotechnology*, vol. 17, no. 11, pp. 2783–2788, Jun. 2006.
- [32] A. G. Roca *et al.*, "Magnetite nanoparticles with no surface spin canting," *J. Appl. Phys.*, vol. 105, no. 11, Jun. 2009, Art. no. 114309.
- [33] J. S. Salazar *et al.*, "Magnetic iron oxide nanoparticles in 10–40 nm range: Composition in terms of magnetite/maghemite ratio and effect on the magnetic properties," *Chem. Mater.*, vol. 23, no. 6, pp. 1379–1386, 2011.
- [34] S. P. Schwaminger, D. Bauer, P. Fraga-García, F. E. Wagner, and S. Berensmeier, "Oxidation of magnetite nanoparticles: Impact on surface and crystal properties," *CrystEngComm*, vol. 19, no. 2, pp. 246–255, 2017.
- [35] P. Thompson, D. E. Cox, and J. B. Hastings, "Rietveld refinement of Debye-Scherrer synchrotron X-ray data from Al₂O₃," *J. Appl. Crystallogr.*, vol. 20, no. 2, p. 79, 1987.
- [36] E. J. W. Verwey and P. W. Haayman, "Electronic conductivity and transition point of magnetite (Fe₃O₄)," *Physica*, vol. 8, no. 9, pp. 979–987, 1941.
- [37] F. Walz, "The verwey transition—A topical review," *J. Phys., Condens. Matter*, vol. 14, no. 12, pp. R285–R340, Apr. 2002.
- [38] J. Wang, Q. Chen, X. Li, L. Shi, Z. Peng, and C. Zeng, "Disappearing of the Verwey transition in magnetite nanoparticles synthesized under a magnetic field: Implications for the origin of charge ordering," *Chem. Phys. Lett.*, vol. 390, nos. 1–3, pp. 55–58, May 2004.
- [39] K. Yamamoto, S. Majetich, M. R. McCartney, M. Sachan, S. Yamamuro, and T. Hirayama, "Direct visualization of dipolar ferromagnetic domain structures in Co nanoparticle monolayers by electron holography," *Appl. Phys. Lett.*, vol. 93, no. 8, 2008, Art. no. 082502.
- [40] S. Yamamuro, D. F. Farrell, and S. A. Majetich, "Direct imaging of self-assembled magnetic nanoparticle arrays: Phase stability and magnetic effects on morphology," *Phys. Rev. B, Condens. Matter*, vol. 65, no. 22, Jun. 2002, Art. no. 224431.